9th International Conference on Numerical Ship Hydrodynamics
Ann Arbor, Michigan, August 5-8, 2007

Numerical Modeling of Waves Generated by High-Speed Vessels in Shallow Water with a Coupled Boussinesq-Panel Method

Okey Nwogu (University of Michigan, Ann Arbor, USA)

ABSTRACT

A numerical model is developed to simulate waves generated by high-speed vessels traveling at sub-critical, transcritical and supercritical speeds in shallow water over water of varying depth. The waves in the far field are assumed to be weakly dispersive with wavelengths much longer than the water depth. The vertical profile of the flow field is obtained from a second-order Taylor series expansion of the velocity potential about an arbitrary elevation in the water column. The velocity potential in the region near the ship is decomposed into a far-field potential, that is valid throughout the computational domain, and a local near-field body potential that decays rapidly away from the body. The boundary integral method is used to solve for the near-field body potential. The formulation leads to a fully nonlinear set of Boussinesq-type water wave evolution equations with forcing terms from the boundary integral of a source distribution over the body surface in the near field. An eddy viscosity-based formulation is used to simulate energy dissipation due to wave breaking. The resulting system of evolution equations are integrated in time using a finite difference method. Numerical model predictions are compared with data from laboratory experiments on ship-generated waves over a wide range of depth-based Froude numbers ($0.7 < F_h < 2$) in both wide and narrow channels.

INTRODUCTION

With the increasing use of high-speed vessels for ferry operations in shallow and confined waters, there has been growing concern about the impact of waves generated by such vessels on the marine environment. High-speed vessels are capable of operating at speeds of 35 to 45 knots, compared to 10 to 20 knots for conventional vessels. Two critical parameters that govern the wake pattern of moving vessels in shallow waterways are the depth–based Froude number, F_h, which expresses the ratio of the vessel speed to the maximum wave propagation speed in a given water depth, and the blockage ratio, B_r, which is the ratio of the maximum cross-sectional area of the ship to the channel cross-sectional area. Most of the reported problems with high-speed vessels occur in shallow and confined channels where the bottom topography and lateral boundaries significantly modify the ship-induced wave field.

High-speed vessels tend to operate in the transcritical ($F_h \approx 1$) and supercritical ($F_h > 1$) regimes in coastal waters, in contrast to conventional vessels that typically operate at sub-critical ($F_h < 1$) speeds. Vessels traveling at trans-critical and supercritical speeds in narrow confined channels can generate non-dispersive solitary-type waves and turbulent bores that can propagate over large distances. The formation of bores and solitary-type waves becomes less likely as the channel becomes wider. However, the super-critical wake pattern in wide channels includes long period [O(10s)] waves at the leading edge of the wake. The long-period waves could pose a problem in sheltered waterways not typically exposed to long period wind-generated waves. These swell-type waves, which are barely visible in deep water, can be amplified and focused by bathymetric features in shallow water.

A number of numerical models have been developed to predict the wave field generated by moving vessels. These models can be loosely classified into near-field models, which resolve details of the flow field near the ship but are too computationally intensive to extend to regions far away from the ship, and far-field models, which simulate the propagation and transformation of ship-generated waves at large

distances away from the ship but have a poorer description of the flow near the ship. Most near-field models are based on boundary integral equations derived from Green's theorem, where the velocity potential associated with the fluid and body motions is represented by a distribution of point sources over the immersed body surface and free surface (e.g. Beck *et al*., 1993). Near-field models can be computational intensive if applied over large coastal areas where the seabed has to be discretized in addition to free surface and ship hull.

Far-field models solve water wave evolution equations derived by integrating the governing mass and momentum equations over the water depth. For weakly dispersive waves, the vertical profile of the flow field is obtained by expanding the velocity potential, as a Taylor series about an arbitrary elevation in the water column (e.g. Nwogu, 1993). The governing equations are then integrated over the water depth, reducing the three-dimensional problem to a two-dimensional one. Depth-integrated equations represent a computationally efficient tool for simulating the propagation and transformation of nonlinear waves over large areas. The equations are able to describe the transformation of waves due to effects such as shoaling/refraction over variable topography, diffraction/reflection by coastal structures, nonlinear wave-wave interactions, wave breaking and wave-induced currents in the surf zone.

Several investigators have extended weakly dispersive far-field (Boussinesq) models to simulate ship generated waves. Early work in the 1980s used Boussinesq models to investigate the generation of upstream-propagating solitary waves. Ertekin *et al*. (1986), and Wu (1987), both used a moving pressure distribution on the free surface to simulate the effect of a moving ship. The applied pressure distribution, however, does not satisfy the kinematic boundary condition on the ship hull and there is no explicit relationship between the pressure distribution and body boundary condition.

For slender bodies, a different approach to satisfying the body boundary condition is the method of matched asymptotic expansions, in which the boundary condition for the far-field problem is derived from an asymptotic solution of the near-field problem. This technique was initially used by Tuck (1966) to predict the flow field induced by slender ships in shallow water. The ship is represented by a moving distribution of point sources placed along the ship's centerline. Tuck's (1966) solution represents the leading order slender body solution in which the free surface is replaced by a rigid lid in the near field. The outer solution of near-field problem thus represents a depth-uniform streaming flow between two rigid horizontal boundaries, consistent with the use of the depth-uniform shallow water equations in the far field. To model weakly dispersive waves in the far-field, Tuck's asymptotic expansion method would have to be extended to higher orders to be consistent with the second-order Boussinesq expansion in the far-field for dispersive waves.

In this paper, we adopt a different approach to satisfying the body boundary condition while maintaining the computational efficiency of depth-integrated Boussinesq-type models. Instead of asymptotically expanding the near-field solution, we directly couple the Boussinesq equations in the far field with a 3-D near-field boundary integral solution that satisfies the boundary conditions on the immersed body surface. The time-dependent evolution of the free surface elevation in the near field is still governed by the Boussinesq equations with the boundary-integral solution providing a forcing term. The numerical model is validated with two sets of data from laboratory experiments conducted over a wide range of depth-based Froude numbers in the sub-critical, trans-critical and supercritical regimes in both a wide and narrow channel.

THEORETICAL FORMULATION

Consider a ship moving at speed $\boldsymbol{U}$ in a navigation channel of variable water depth, h. A fixed Cartesian coordinate system is adopted with (x,y) the horizontal plane at the still water level and z measured vertically upwards. The fluid is assumed to be incompressible and inviscid with the fluid motion described by a velocity potential, $\Phi(x,y,z,t)$. The fluid has to satisfy the continuity (Laplace) equation in the bounded fluid volume, V, subject to boundary conditions at the free surface, seabed and body surface, S_B:

$$\nabla^2\Phi + \Phi_{zz} = 0 \qquad \text{in } V \tag{1}$$

$$\eta_t + \nabla\Phi\cdot\nabla\eta - \Phi_z = 0 \qquad \text{at } z=\eta \tag{2}$$

$$\Phi_t + g\eta + \frac{1}{2}\left(\nabla\Phi\cdot\nabla\Phi + \Phi_z^2\right) = 0 \qquad \text{at } z=\eta \tag{3}$$

$$\nabla\Phi\cdot\nabla h + \Phi_z = 0 \qquad \text{at } z=-h \tag{4}$$

$$\nabla\Phi\cdot\boldsymbol{n} + \Phi_z n_z = \boldsymbol{U}\cdot\boldsymbol{n} \qquad \text{on } S_B \tag{5}$$

where $(\boldsymbol{n},n_z)$ is the unit outward normal vector to the body surface and $\nabla=(\partial/\partial x,\partial/\partial y)$. The lateral boundaries of the computational domain are assumed to be fully reflecting with outgoing waves absorbed in damping layers placed next to the wall boundaries. To solve the initial/boundary problem, we divide the computational domain into two regions: the near-field region close to

the ship and the far-field region, far away from the ship.

Far-Field Solution

Since we are primarily interested in ship-generated waves in shallow water, we assume that that the waves in the far field are weakly dispersive. The vertical structure of the flow field in the far field is thus obtained by expanding the velocity potential, Φ, as a Taylor series about an arbitrary elevation, z_α, in the water column (Nwogu, 1993). This corresponds to an asymptotic expansion of the velocity field in terms of a frequency dispersion parameter, $\mu = h/L$ (where L is the wavelength). The zeroth order approximation corresponds to non-dispersive shallow water waves while the second-order [$O(\mu^2)$] expansion corresponds to weakly dispersive waves with a quadratic variation of the velocity potential over depth:

$$\begin{aligned}\Phi^{(F)}(\boldsymbol{x},z,t) = \phi_\alpha &+ \frac{1}{2}\mu^2\left[(z_\alpha+h)^2-(z+h)^2\right]\nabla^2\phi_\alpha \\ &+ \mu^2\,(z_\alpha - z)\left[\nabla\phi_\alpha\cdot\nabla h\right] + O(\mu^4)\end{aligned} \tag{6}$$

where $\phi_\alpha = \Phi(\boldsymbol{x},z_\alpha,t)$. The above expansion satisfies the Laplace equation (Eqn. 1) and the seabed boundary condition (Eqn. 4). The horizontal and vertical velocities are obtained from the velocity potential as:

$$\begin{aligned}\boldsymbol{u}(\boldsymbol{x},z,t) = \boldsymbol{u}_\alpha &+ (z_\alpha - z)\left[\nabla(\boldsymbol{u}_\alpha\cdot\nabla h)+(\nabla\cdot\boldsymbol{u}_\alpha)\nabla h\right] \\ &+ \frac{1}{2}\left[(z_\alpha+h)^2-(z+h)^2\right]\nabla(\nabla\cdot\boldsymbol{u}_\alpha)\end{aligned} \tag{7}$$

$$w(\boldsymbol{x},z,t) = -\left[\boldsymbol{u}_\alpha\cdot\nabla h + (z+h)\nabla\cdot\boldsymbol{u}_\alpha\right] \tag{8}$$

where $\boldsymbol{u}_\alpha = \nabla\Phi|_{z_\alpha}$ is the horizontal velocity at $z = z_\alpha$. Given a vertical profile for the flow field, the mass and momentum equations can be integrated over depth, reducing the three-dimensional problem to a two-dimensional one. The mass conservation equation is obtained by integrating the Laplace equation (Eqn. 1) over the water depth and applying the kinematic boundary conditions at the seabed and free surface to yield:

$$\eta_t + \nabla\cdot\left[(h+\eta)\bar{\boldsymbol{u}}\right] = 0 \tag{9}$$

where $\bar{\boldsymbol{u}}$ is the depth-averaged horizontal velocity given by:

$$\begin{aligned}\bar{\boldsymbol{u}} = \frac{1}{h+\eta}\int_{-h}^{\eta}\boldsymbol{u}\,dz &= \boldsymbol{u}_\alpha \\ &+ \left[(z_\alpha+h)-\frac{(h+\eta)}{2}\right]\left[\nabla(\boldsymbol{u}_\alpha\cdot\nabla h)+(\nabla\cdot\boldsymbol{u}_\alpha)\nabla h\right] \\ &+ \left[\frac{(z_\alpha+h)^2}{2}-\frac{(h+\eta)^2}{6}\right]\nabla(\nabla\cdot\boldsymbol{u}_\alpha)\end{aligned} \tag{10}$$

The horizontal gradient of the dynamic free surface boundary condition (Eqn. 3) can be written as:

$$\boldsymbol{u}_t|_\eta + w_t|_\eta\,\nabla\eta + g\nabla\eta + \left(\boldsymbol{u}_\eta\cdot\nabla\right)\boldsymbol{u}_\eta + w_\eta\nabla w_\eta = 0 \tag{11}$$

where $\boldsymbol{u}_\eta = \boldsymbol{u}(\boldsymbol{x},\eta,t)$, $w_\eta = w(\boldsymbol{x},\eta,t)$ are the horizontal and vertical velocities at the free surface. By substituting equations (7) and (8) into (11), we obtain the momentum equation as evolution equation for the horizontal velocity variable $\boldsymbol{u}_\alpha$:

$$\begin{aligned}&\boldsymbol{u}_{\alpha,t} + g\nabla\eta + \left(\boldsymbol{u}_\eta\cdot\nabla\right)\boldsymbol{u}_\eta + w_\eta\nabla w_\eta \\ &+ (z_\alpha-\eta)\left[\nabla\left(\boldsymbol{u}_{\alpha,t}\cdot\nabla h\right)+(\nabla\cdot\boldsymbol{u}_{\alpha,t})\nabla h\right] \\ &+ \frac{1}{2}\left[(z_\alpha+h)^2-(h+\eta)^2\right]\nabla\left(\nabla\cdot\boldsymbol{u}_{\alpha,t}\right) \\ &- \left[\left(\boldsymbol{u}_{\alpha,t}\cdot\nabla h\right)+(h+\eta)\nabla\cdot\boldsymbol{u}_{\alpha,t}\right]\nabla\eta \\ &+ \frac{1}{h+\eta}\nabla(\nu(h+\eta)\nabla\cdot\boldsymbol{u}_\alpha)+\frac{1}{h+\eta}f_b\boldsymbol{u}_b|\boldsymbol{u}_b| = 0\end{aligned} \tag{12}$$

where $\boldsymbol{u}_b = \boldsymbol{u}(\boldsymbol{x},-h,t)$ is the horizontal velocity at the seabed. The equations also include empirical terms to account for wave energy dissipation due to bottom friction and turbulent processes, with f_b an empirical bottom friction coefficient and ν an eddy viscosity coefficient. A Smagorinsky-type formulation is adopted for sub-grid turbulent processes with the eddy viscosity coefficient proportional to the velocity gradients and the grid size, i.e.:

$$\nu = C_s^2\Delta x\Delta y\left[\left(u_{\alpha,x}\right)^2+\left(v_{\alpha,y}\right)^2+\frac{1}{2}\left(u_{\alpha,y}+v_{\alpha,x}\right)^2\right]^{1/2} \tag{13}$$

where C_s is the Smagorinsky constant. The eddy viscosity term is also used to describe energy dissipation due to wave breaking.

The elevation of the velocity variable z_α is a free parameter that is chosen to minimize differences between the linear dispersion characteristics of system of equations and the exact dispersion relation for small amplitude waves and is given by $z_\alpha = -0.535h$ (Nwogu, 1993).

Near-Field Solution

To provide a seamless transition between the near-field and far-field problems, we decompose the total velocity potential in the near field into the far-field potential given by equation (6) and a near-field body potential, $\Phi^{(B)}$, which represents a perturbation to the far-field potential due to the presence of the body:

$$\Phi = \Phi^{(B)} + \Phi^{(F)} \tag{14}$$

The above decomposition automatically imposes the boundary condition:

$$\nabla\Phi^{(B)}, \Phi_z^{(B)} \to 0 \text{ as } \boldsymbol{x} \to \infty \tag{15}$$

at the matching boundary between the near-field and far-field regions. The total velocity potential in the near-field has to satisfy the Laplace equation and the boundary conditions given by equation (2) to (5):

$$\nabla^2\Phi^{(B)} + \Phi_{zz}^{(B)} = 0 \qquad \text{in } V \tag{16}$$

$$\eta_t + \nabla\Phi^{(F)} \cdot \nabla\eta - \Phi_z^{(F)} = \Phi_z^{(B)} - \nabla\Phi^{(B)} \cdot \nabla\eta \text{ at } z = \eta \tag{17}$$

$$\begin{aligned} &\Phi_t^{(F)} + \Phi_t^{(B)} + g\eta + \frac{1}{2}\left(\Phi_z^{(F)} + \Phi_z^{(B)}\right)^2 \\ &\frac{1}{2}\left(\nabla\Phi^{(F)} + \nabla\Phi^{(B)}\right)\cdot\left(\nabla\Phi^{(F)} + \nabla\Phi^{(B)}\right) = 0 \quad \text{at } z = \eta \end{aligned} \tag{18}$$

$$\nabla\Phi^{(F)} \cdot \nabla h + \Phi_z^{(F)} = -\nabla\Phi^{(B)} \cdot \nabla h - \Phi_z^{(B)} \qquad \text{at } z = -h \tag{19}$$

$$\frac{\partial\Phi^{(B)}}{\partial n} = \left(\boldsymbol{U} - \nabla\Phi^{(F)}\right)\cdot\boldsymbol{n} - \Phi_z^{(F)} n_z \qquad \text{on } S_B \tag{20}$$

The solution of the initial-boundary value problem for the body potential $\Phi^{(B)}$ can be obtained by integrating the kinematic and dynamic free surface boundary conditions (Eqns. 17 & 18) in time, and using the boundary integral method to solve the Laplace equation to close the system of equations at each time step (e.g. Beck *et al*., 1993). However, we choose to solve a simplified form of the body potential problem. We avoid solving the time-dependent momentum equation (Eqn. 18) for the body potential at the free surface by imposing the boundary condition:

$$\Phi^{(B)} = 0 \qquad \text{at } z = 0 \tag{21}$$

Since $\Phi^{(B)}$ represents a perturbation to $\Phi^{(F)}$ in the near field, the boundary condition is applied at $z = 0$ instead of $z = \eta$. We also assume that the water depth is uniform in the near-field region and replace Eqn. (19) with:

$$\Phi_z^{(B)} = 0 \qquad \text{at } z = -h \tag{22}$$

At any instant of time, the solution of Eqn. (16) subject to boundary conditions (15), (20), (21) and (22) can be obtained using a boundary integral of sources on the immersed body surface:

$$\Phi^{(B)}(\boldsymbol{x}, z) = \int_{S_B} \sigma(\boldsymbol{x}', z') G(\boldsymbol{x}, z; \boldsymbol{x}', z')\, dS \tag{23}$$

where $G(\boldsymbol{x},z;\boldsymbol{x}',z')$ a Green's function that satisfies the Laplace equation and boundary conditions at the free surface (21), seabed (22) and radiation boundary (15), $\sigma(\boldsymbol{x}',z')$ are the unknown source strengths, $(\boldsymbol{x},z)$ is the field point at which the velocity potential is evaluated and $(\boldsymbol{x}',z')$ is the source location. The Green's function is given by the method of images as:

$$\begin{aligned} G(\boldsymbol{x}, z; \boldsymbol{x}', z') = &\frac{1}{r} - \frac{1}{r_1} \\ &+ \sum_{m=1}^{\infty} (-1)^m \left(-\frac{1}{r_{2,m}} + \frac{1}{r_{3,m}} - \frac{1}{r_{4,m}} + \frac{1}{r_{5,m}} \right) \end{aligned} \tag{24}$$

where

$$\begin{aligned} r &= \sqrt{(x-x')^2 + (y-y')^2 + (z-z')^2} \\ r_1 &= \sqrt{(x-x')^2 + (y-y')^2 + (z+z')^2} \\ r_{2,m} &= \sqrt{(x-x')^2 + (y-y')^2 + (z+z'+2mh)^2} \\ r_{3,m} &= \sqrt{(x-x')^2 + (y-y')^2 + (z-z'-2mh)^2} \\ r_{4,m} &= \sqrt{(x-x')^2 + (y-y')^2 + (z+z'-2mh)^2} \\ r_{5,m} &= \sqrt{(x-x')^2 + (y-y')^2 + (z-z'+2mh)^2} \end{aligned} \tag{25}$$

The strengths of the sources are determined to satisfy the boundary condition (Eqn. 20) on the body surface. Evaluating the normal derivative of (23) on S_B yields:

$$\begin{aligned} \frac{\partial\Phi^{(B)}}{\partial n}(\boldsymbol{x}, z) = &-2\pi\sigma(\boldsymbol{x}, z) \\ &+ \int_{S_B} \sigma(\boldsymbol{x}', z') \frac{\partial G}{\partial n}(\boldsymbol{x}, z; \boldsymbol{x}', z')\, dS \end{aligned} \tag{26}$$

The above integral equation is solved using the constant panel method. The ship hull is discretized into a finite number of panels with the source strength distribution assumed to be uniform over each panel. The kinematic body boundary condition is then applied at the centroid of each panel to yield a matrix equation for the unknown source strengths. For slender ships, the matrix is diagonally dominant and the source strengths can be approximated by:

$$\sigma = -\frac{1}{2\pi}\left[\left(\boldsymbol{U} - \nabla\Phi^{(F)}\right)\cdot\boldsymbol{n} - \Phi_z^{(F)} n_z\right] \tag{27}$$

The modified kinematic free surface boundary in the near field is obtained by substituting the vertical velocity associated with sources into Eqn. (17):

$$\begin{aligned}&\eta_t + \nabla\Phi^{(F)}\cdot\nabla\eta - \Phi_z^{(F)} = \\ &-\frac{1}{2\pi}\int_{S_B}\left[\left(\boldsymbol{U} - \nabla\Phi^{(F)}\right)\cdot\boldsymbol{n} - \Phi_z^{(F)} n_z\right]\left.\frac{\partial G}{\partial z}\right|_{z=0} dS\end{aligned} \tag{28}$$

where

$$\left.\frac{\partial G}{\partial z}\right|_{z=0} = -2\frac{z'}{r^3} - 2\sum_{m=1}^{\infty}(-1)^m\left(\frac{z'+2mh}{r_{2,m}^3} + \frac{z'-2mh}{r_{4,m}^3}\right) \tag{29}$$

By integrating the Laplace equation over the water depth and applying the kinematic boundary conditions at the free surface and seabed, we obtain a modified depth-integrated mass conservation equation for the near-field region as:

$$\begin{aligned}&\eta_t + \nabla\cdot\left[\left(h+\eta\right)\bar{\boldsymbol{u}}^{(F)}\right] = \\ &-\frac{1}{2\pi}\int_{S_B}\left[\left(\boldsymbol{U} - \boldsymbol{u}^{(F)}\right)\cdot\boldsymbol{n} - w^{(F)} n_z\right]\left.\frac{\partial G}{\partial z}\right|_{z=0} dS\end{aligned} \tag{30}$$

The numerical solution of the near-field problem has thus been reduced to solving a coupled set of Boussinesq-type mass and momentum equations (Eqns. 12 & 30) with a forcing term in the mass equation due to the source distribution over the body surface. For slender bodies, the source strength is proportional to the relative normal velocity on the body. For arbitrarily-shaped bodies, a matrix equation would have to be solved for the unknown source strengths.

The present formulation can be considered equivalent to representing a moving three-dimensional body in the far-field Boussinesq model with a spatial distribution of the vertical velocities induced by the motion of the ship. A *vertical* velocity boundary condition is thus applied at the still water level over a limited region near the ship in contrast to the classical matched-asymptotic slender-body approach of Tuck (1966), where the ship is shrunk to a line and a *horizontal* velocity boundary condition is applied along the ship's centerline.

Although the Green's function is represented by an infinite series, the influence of the image sources decrease with increasing distance from the still water level and the series can be truncated after a finite number of terms. Since the source-induced vertical velocities are proportional to z'/r^3, one practical guideline adopted in this paper is to truncate the series when the ratio of the vertical velocity induced the by the image sources is less than 1% of that induced by the primary source. For a vessel with draft, D, this would correspond to image sources located within $\pm 10D$ of the still water level. Shallow-draft vessels with drafts less than 10% of the water depth can thus be effectively represented by the primary source and its image sink above the still water level.

Wave Breaking

Waves generated by high-speed vessels tend to break around the hull. The effect of wave breaking has been parameterized in the momentum equation (Eqn. 12) with an artificial eddy viscosity term. This term is designed to reproduce the overall wave energy dissipation due to breaking but not details of the turbulent motion. A conceptual breaking model is still required to define the onset of breaking and the post-breaking spatial and temporal evolution of the eddy viscosity. In this paper, we adopt the approach of Nwogu (1996) for spilling breaking waves that is based on the one-equation turbulence closure model used for the Navier-Stokes equations. The eddy viscosity coefficient ν is related to the kinetic energy of the large-scale eddy motions, k, and an eddy length scale, l, by:

$$\nu = \sqrt{k}\,l \tag{31}$$

A one-dimensional transport equation is used to describe the production, advection, diffusion, and dissipation of the eddy kinetic energy:

$$k_t + \boldsymbol{u}_\eta\cdot\nabla k = P - D + \sigma\nu\nabla^2 k \tag{32}$$

where σ is an empirical diffusion constant, and P and D are terms for the production and dissipation of eddy kinetic energy respectively. The breaking model assumes that eddies are generated in the near-surface region and primarily advected with the horizontal velocity at the free surface. The rate of production of the eddy kinetic energy is assumed to be proportional to the vertical gradient of the velocity at the free surface, i.e.:

$$P = B\frac{l^2}{\sqrt{C_D}}\left[\boldsymbol{u}_{z,\eta}\cdot\boldsymbol{u}_{z,\eta}\right]^{3/2} \tag{33}$$

where C_D is an empirical constant and the velocity gradient $\boldsymbol{u}_{z,\eta}$ is given by:

$$\boldsymbol{u}_{z,\eta} = -\left[\nabla(\boldsymbol{u}_\alpha\cdot\nabla h) + (\nabla\cdot\boldsymbol{u}_\alpha)\nabla h\right] - \left(h+\eta\right)\nabla(\nabla\cdot\boldsymbol{u}_\alpha) \tag{34}$$

The parameter B is introduced to ensure that eddy generation occurs after the waves break. Nwogu (1996) used a breaking criterion based on the ratio of the horizontal component of the orbital velocity at the free surface, $\boldsymbol{u}_\eta$, to the phase velocity of the waves, C. For supercritical bores in narrow channels, a Froude-number based criterion appears to be more relevant (e.g. Gourlay, 2001):

$$B = \begin{cases} 0 & \sqrt{g(h+\eta)} < 1.265\sqrt{gh} \\ 1 & \sqrt{g(h+\eta)} >= 1.265\sqrt{gh} \end{cases} \quad (34)$$

The last unknown term in the breaking model is the rate of dissipation of eddy kinetic energy. We assume that it follows the standard 3/2 decay law, i.e.:

$$D = C_D \frac{k^{3/2}}{l} \quad (35)$$

The following values were adopted for the empirical constants: $C_D = 0.08$ and $\sigma = 0.2$, as recommended by Nwogu (1996). The eddy length scale, l, remains the only free parameter in the breaking model and it is typically chosen to be of the order of the wave height.

NUMERICAL SOLUTION

The computational domain represents a numerical towing tank and is discretized as a uniform rectangular grid with grid sizes Δx and Δy, in the x and y directions, respectively. The prognostic variables η and $\boldsymbol{u}_\alpha$ are defined at the grid points in a staggered manner with the surface elevation defined at the grid nodes while the velocities are defined half a grid point on either side of the elevation grid points. The governing mass and momentum equations are integrated in time using a modified third-order accurate Crank-Nicholson scheme (Nwogu, 1993). The partial derivatives are approximated using a forward difference scheme for time and central difference schemes for the spatial derivatives. Details of the numerical scheme are provided in Nwogu and Demirbilek (2001).

At each time step, we solve an algebraic expression for the change in η at all grid points and tri-diagonal matrix equations for changes to u_α and v_α along lines in the x and y directions, respectively. Identical mass and momentum equations are solved in both the near and far fields with the additional contribution of the boundary integral of the source distribution over the body surface due to the motion of the ship evaluated over a limited spatial region, defined to be half a ship length for all the simulations in this paper. A linear interpolation scheme is used to evaluate the far-field fluid velocities at the centroids of the panels. The ship is then moved to its new position at the next time step and the calculations repeated at the next time step.

Waves propagating out of the computational domain can be optionally absorbed in damping regions placed around the perimeter of the computational domain. Artificial dissipation of wave energy in damping layers is achieved through the introduction of a term proportional to the surface elevation into the right-hand side of the mass equation:

$$F_{d\eta} = -\mu(\boldsymbol{x})\,\eta \quad (36)$$

and a term proportional tangential velocity at the free surface into the right-hand side of the momentum equation:

$$F_{du} = -\mu(\boldsymbol{x})\left(\boldsymbol{u}_\eta + w_\eta \nabla \eta\right) \quad (37)$$

where $\mu(\boldsymbol{x})$ is the damping strength with that varies quadratically within the damping layer with a maximum value of $30/T$ at the wall boundary, where T is a characteristic wave period.

LABORATORY EXPERIMENTS IN A WIDE BASIN

Doctors (2003) carried out an extensive series of laboratory experiments in a wide basin to investigate the wavemaking characteristics of a model catamaran. The experiments were conducted in the model basin of the Australian Maritime College. The basin is 35 m long, 12 m wide and can support water depths up to 1m.

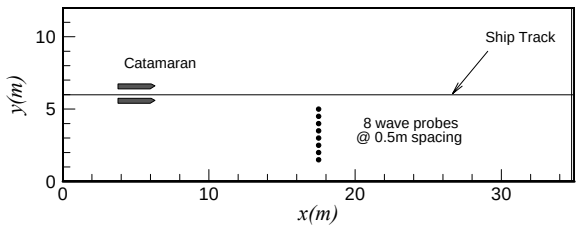

Figure 1: Layout of laboratory experiments of Doctors (2003)

A model catamaran was built from a modified Series 64 high-speed displacement parent hull form (Yeh, 1965) with a transom stern. The hulls were each 1.5 m long with a beam of 0.1113 m, draft of 0.04623 m and block coefficient of 0.49. The model was towed along the centerline of the basin (y = 6m) as shown in Figure 1. Eight probes were used to measure the water surface elevation along a transect at x = 17.5m. The probes

were uniformly spaced at an interval of 0.5 m with Probe #1 located at y = 5m (or 1 m from the ship track) and Probe #8 located at a distance of 1.5m from the wall (or 4.5 m from the ship track).

A total of 156 experiments were conducted with three different demihull spacings, four different water depths and thirteen different ship speeds. In this paper, we focus on a limited subset of those experiments with a water depth of 0.45 m, a demihull spacing of 0.4 m, and four non-dimensional ship speeds with depth-based Froude numbers ranging from 0.73 to 1.79.

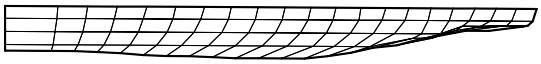

Figure 2: Side view of discretized catamaran hull form.

Each hull of the catamaran was discretized with 168 quadrilateral panels as shown in Figure 2. We initially investigated the spatial distribution of the vertical velocities induced by the body singularities. Figure 3 shows a plot of the vertical velocity field normalized by its maximum value. As expected, the vertical velocities induced by the ship motion are strongest near the ship's waterline in regions where the component of the normal vector in the direction of ship motion (n_x) is largest near the bow and transom stern. A plot of the normalized velocity field along a y-transect at x = 1.5 m (or x/L = 0.67 from stern) is shown in Figure 4. It can be seen that vertical velocity field decays rapidly away from the body to less than 10^{-5} of its maximum value at distance of half a ship length from the body. We thus used half a ship length as a reasonable upper limit to define the extent of the near-field region.

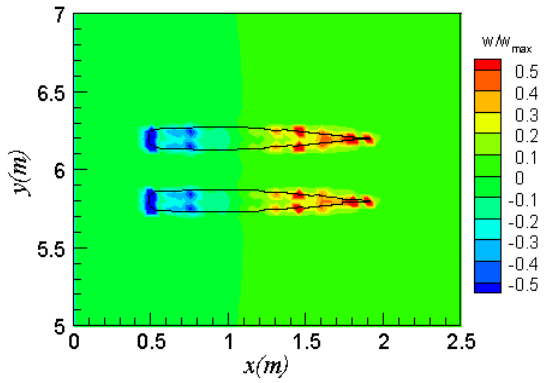

Figure 3: Spatial distribution of normalized vertical velocity field induced by motion of ship.

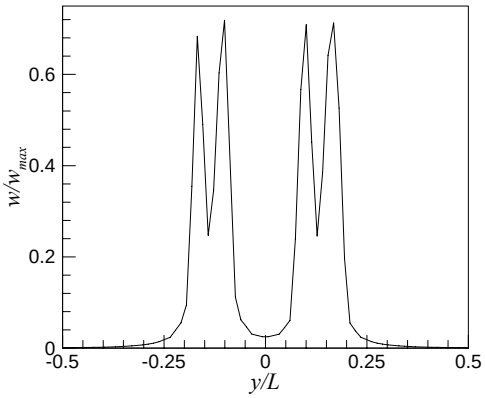

Figure 4: Normalized vertical velocity field induced by motion of ship along x/L = 0.67 from stern.

The numerical model basin was setup to reproduce the configuration of laboratory model basin. A 35 m long, 12 m wide and 0.45 m deep computational domain was set up with grid sizes $\Delta x = \Delta y$ = 0.05m for a total of 701 points in the x direction and 241 points in the y direction. The lateral boundaries were fully reflecting while 0.5 m wide damping layers were placed at the upstream and downstream ends of the basin to absorb outgoing waves.

Numerical simulations were carried out for model ship speeds of 1.533 m/s, 1.917 m/s, 3.067 m/s, and 3.757 m/s, corresponding to depth-based Froude F_h = 0.73, 1.0, 1.47 and 1.79. The simulations were performed with time step size Δt =0.015s, Smagorinsky coefficient C_s = 0.2 and bottom friction coefficient f_b = 0.01. Sample snapshots of the instantaneous water surface elevation are plotted in Figures 5 to 8 for F_h = 0.73, 1.0, 1.47 and 1.79 respectively. For vessels traveling at subcritical speeds in deep water, the classical V-shaped Kelvin ship water pattern is obtained with a wake consisting of diverging and transverse waves enclosed within 19.5° cusp lines. As the water depth decreases, the half-angle of the enclosing wedge slowly increases to 90° at F_h = 1 before decreasing again in the supercritical regime.

Havelock (1908) derived the relationship between the wedge half-angle and depth-based Froude number as:

$$\beta = \begin{cases} \cos^{-1}\left(\dfrac{\sqrt{8(1-n)}}{3-n}\right) & F_h < 1 \\ \sin^{-1}\left(\dfrac{1}{F_h}\right) & F_h \geq 1 \end{cases} \qquad (39)$$

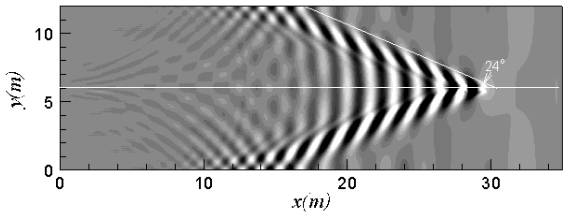

Figure 5: Predicted wave pattern for a vessel travelling at Froude Number, $F_h = 0.73$.

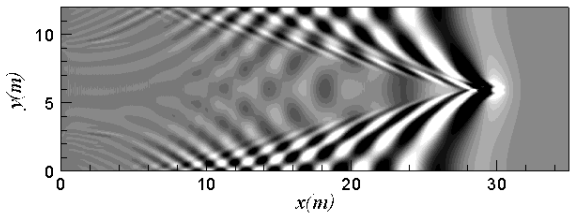

Figure 6: Predicted wave pattern for a vessel travelling at Froude Number, $F_h = 1.0$.

where

$$n = \frac{2}{F_h^2 \sinh\left(2/F_h^2\right)} \tag{40}$$

The predicted enclosing half-wedge angles are 24°, 43° and 34° for $F_h = 0.73$, 1.47 and 1.79 respectively. The theoretical half-wedge angles for are also shown in Figures 5, 7 & 8. It can be seen that the theoretically-predicted angles visually correlate well with the simulated wake pattern.

Figures 5 to 8 also highlight the differences in the sub-critical (F_h = 0.73), transcritical (F_h = 1), and supercritical (F_h = 1.47, 1.79) wake patterns. At sub-critical speeds, the wake still consists of the classical diverging and transverse waves. At $F_h \approx 1$, the transverse waves are barely able to keep up with the ship and decay rapidly in height away from the stern. At supercritical speeds, the wake consists of a sequence of diverging waves with the longest wave at the leading edge of the V-shaped wake. The wavelength/wave period of the trailing diverging waves decrease as the wave propagation angle becomes more aligned with the ship track.

We next conducted detailed model-data comparisons of the time histories of the water surface elevation at the laboratory gauge locations. Figures Figures 9 to 12 show a comparison of the measured and predicted time histories at Probes #1 (1m from ship track), #3 (2m from ship track) and #7 (4m from ship track).

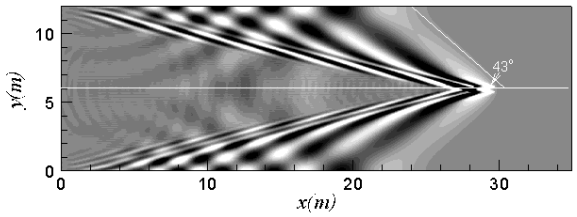

Figure 7: Predicted wave pattern for a vessel travelling at Froude Number, $F_h = 1.47$.

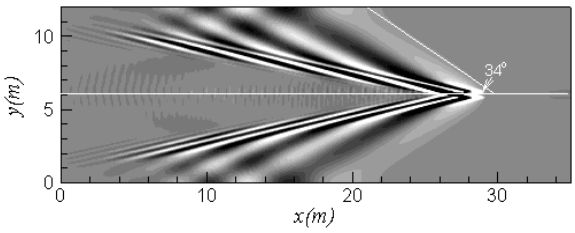

Figure 8: Predicted wave pattern for a vessel travelling at Froude Number, $F_h = 1.79$.

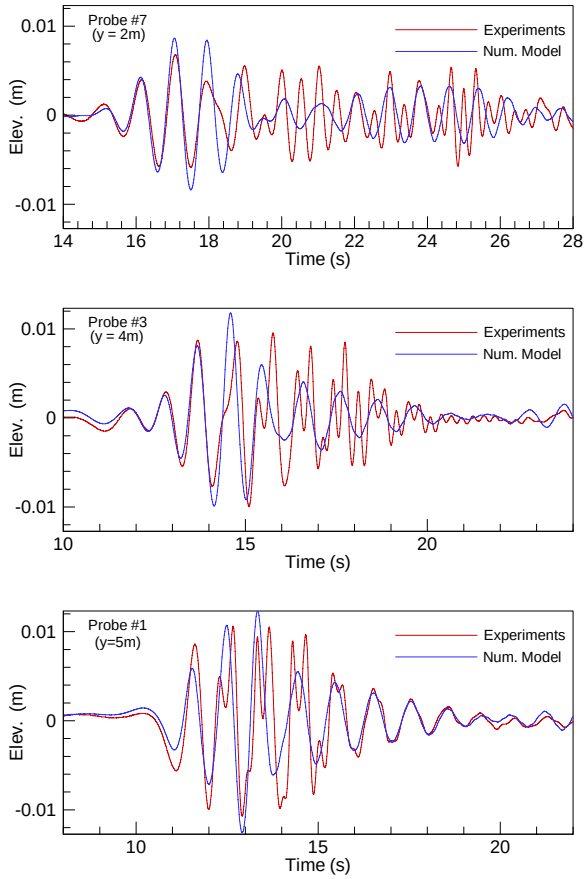

Figure 9: Comparison of time histories of the measured and predicted free surface elevations at Probes #1, #3 and #7 for a vessel travelling at Froude Number, $F_h = 0.73$.

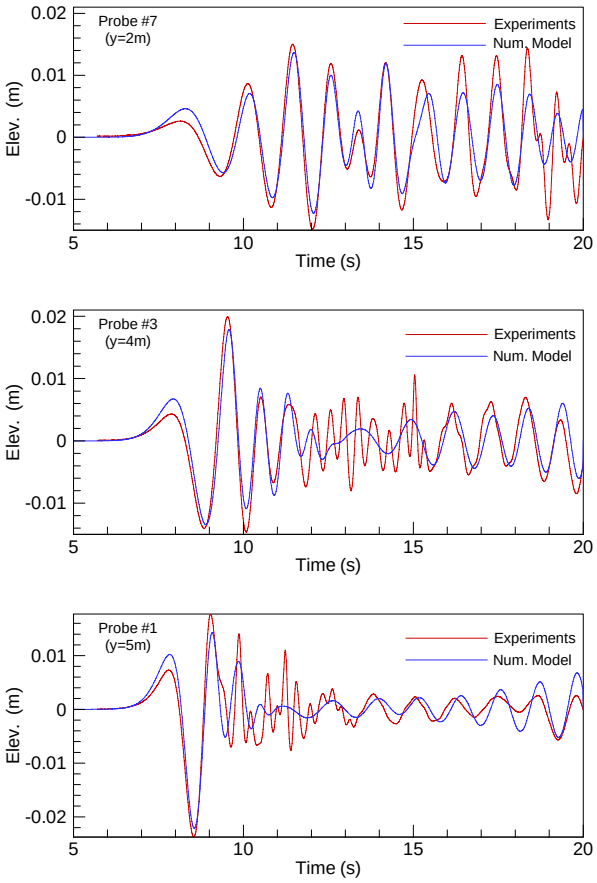

Figure 10: Comparison of time histories of the measured and predicted free surface elevations at Probes #1, #3 and #7 for a vessel travelling at Froude Number, $F_h = 1.0$

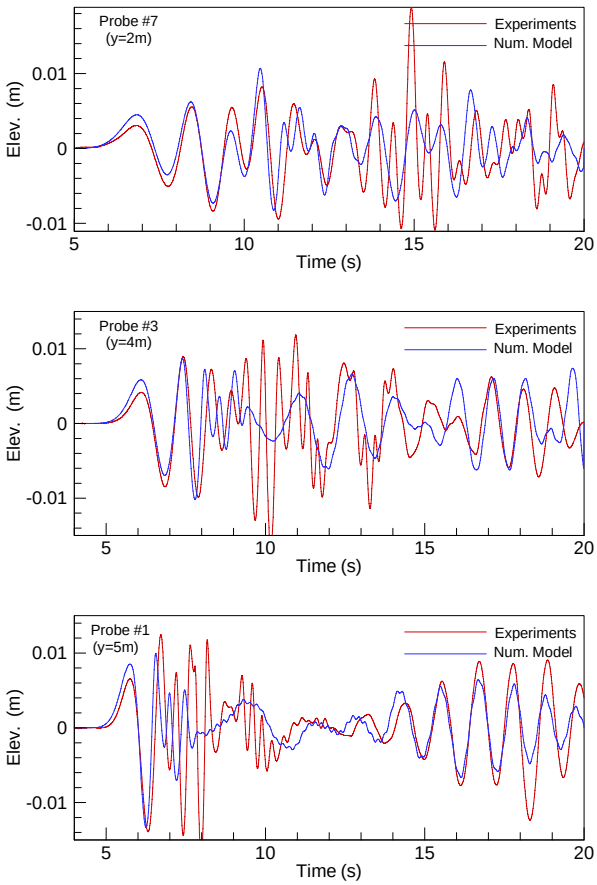

Figure 11: Comparison of time histories of the measured and predicted free surface elevations at Probes #1, #3 and #7 for a vessel travelling at Froude Number, $F_h = 1.47$.

For the sub-critical ($F_h = 0.73$) test, the ship-generated wave time histories look like dispersive wave packets. Good agreement is generally observed between the measured and numerically-predicted time histories except for the presence of high-frequency fluctuations in the measured data. The high-frequency fluctuation corresponds to diverging waves with periods of 0.33s or water depth to wavelength ratio $h/L = 2.65$. These extremely short-period waves are beyond the dispersive limit of the Boussinesq model (max $h/L = 0.5$) and cannot be resolved by the weakly dispersive model. We should also point out that the wave periods are related to the ship speed and wave propagation direction by the dispersion relation:

$$U\cos\theta = \frac{2\pi}{kT} = \sqrt{\frac{g}{k}\tanh kh} \qquad (41)$$

where k is the wavenumber and θ is the wave direction relative to ship track with θ = 0° corresponding to transverse waves propagating parallel to the ship track.

The dominant transverse wave for $F_h = 0.73$ with θ = 0° has a wave period $T = 1.04$s while the dominant diverging wave close to the cusp line with θ = 34° has a period of 0.82s. The high-frequency fluctuations in the measured data (T=0.33s) correspond to short diverging waves in the inner region of the wake with wave direction θ = 70°, which is almost perpendicular to the ship track. These waves would typically be damped out in prototype by the turbulence from the propulsion system.

The model-data comparisons are shown in Figure 10 for the transcritical speed $F_h = 1.0$. A prominent depression of the water level is observed at Probe #1 which is closest to the ship. This lowering of the water level is a "Bernoulli" effect, associated with the increase in fluid velocity as the flow accelerates around the hull. The magnitude of the depression decreases with increasing distance from the ship track and is barely noticeable at the far-field gauge (Probe #7). Reasonably good agreement is also observed between the numerical model predictions and measured data except for the extremely short-period diverging waves.

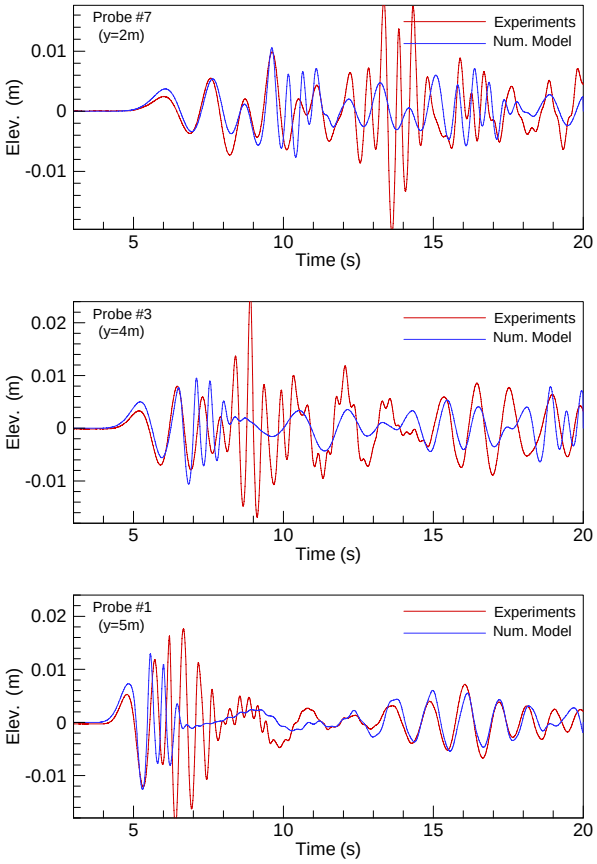

Figure 12: Comparison of time histories of the measured and predicted free surface elevations at Probes #1, #3 and #7 for a vessel travelling at Froude Number, $F_h = 1.79$.

The supercritical wave pattern includes a broader band of wave frequencies from long-period waves at the leading edge to short-period waves in the inner region of the wake. Some of the largest waves in the measured time histories shown in Figures 11 and 12 for $F_h = 1.47$ and 1.79 correspond to the extremely-short diverging waves. The weakly dispersive Boussinesq model is able to match the first few long-period waves but not the shorter trailing waves.

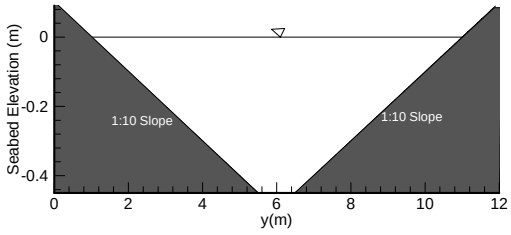

Figure 12: Cross-sectional profile of bathymetry of navigation channel used for the ship wave shoaling tests.

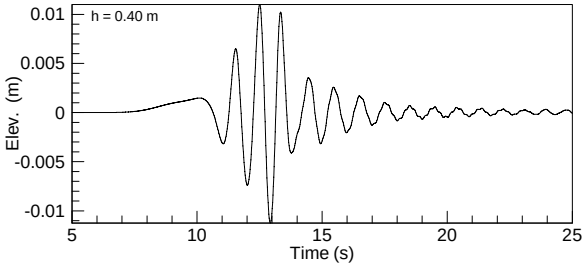

Figure 14: Predicted free surface elevation time history at y = 5m (h = 0.4m) for a vessel travelling at Froude Number, F_h = 0.73.

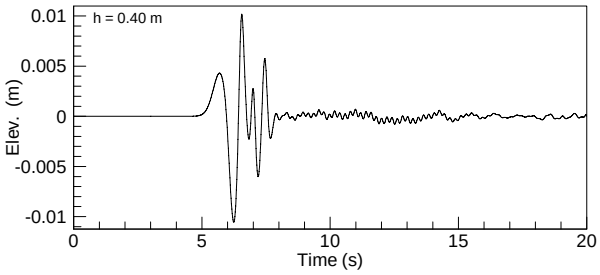

Figure 15: Predicted free surface elevation time history at y = 5m (h = 0.4m) for a vessel travelling at Froude Number, F_h = 1.47.

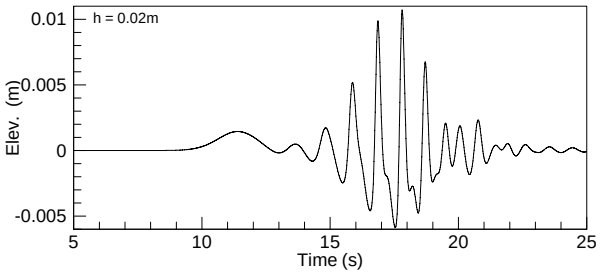

Figure 16: Predicted free surface elevation time history at y = 1.2m (h = 0.02m) for a vessel travelling at Froude Number, F_h = 0.73.

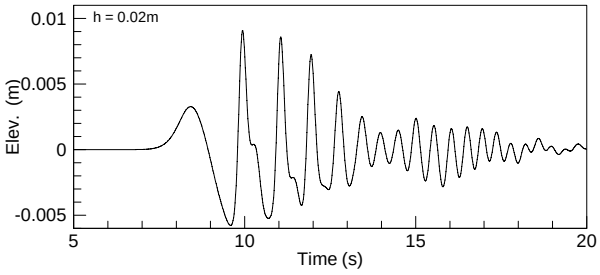

Figure 17: Predicted free surface elevation time history at y = 1.2m (h = 0.02m) for a vessel travelling at Froude Number, F_h = 1.47.

We next investigated differences between the shoaling characteristics of the sub-critical and supercritical wave patterns by building a navigation channel with a 1-m wide constant depth section and side slopes of 1:10 as shown in Figure 13 in the computational basin. A 0.15-m wide damping layer was place along the shoreline to absorb waves running up the beach slope. Numerical tests were repeated for the F_h = 0.73 and F_h = 1.47 ship speeds with the new bathymetry. Figures 14 and 15 show the predicted surface elevation time histories at y = 5m (h = 0.4m). Similar wave heights of ~0.02cm were obtained for both the sub-critical and supercritical speeds at the "deep" section.

Figures 16 and 17 show the predicted wave elevation time histories at a shallow water depth of 0.02m close to the shoreline. Nonlinear wave steepening leads to a highly asymmetric profile in shallow water. Although the asymmetric profiles of the sub-critical and supercritical tests look similar, we notice a distinct difference in the wave front. While the sub-critical pattern is shaped more like a dispersive wave packet with the largest wave in the middle, the supercritical pattern has an *N*-shaped wave front with the largest crest elevation occurring immediately after the initial water level depression. The subsequent waves gradually decrease in height. Supercritical speeds thus lead to large breaking wave event after the initial water level depression. This would be consistent several reported observations of "waves appearing out of nowhere" for high-speed vessel wakes. The *N*-shaped wave front is also similar to that of tsunamis and would lead to larger wave runup on the shoreline.

LABORATORY EXPERIMENTS IN A NARROW TANK

Gourlay (2001) conducted laboratory experiments in the towing tank of the Australian Maritime College to investigate the turbulent bores generated by vessels traveling at supercritical speeds in narrow channels. The tank is 60 m long and 3.5 m wide. The tests were conducted at a water depth of 0.114 m. A monohull vessel with a length of 1.6 m, beam of 0.4 m and draft of 0.1 m was used for the experiments. The parent hull of the vessel is the high-speed displacement hull series described in Robson (1988) with a wide transom stern and rounded bilge.

The extremely large vessel draft to water depth ratio (h/D = 0.114) and wide transom stern of the vessel made this test series more difficult to simulate. We eventually added a virtual appendage to vessel stern as suggested by Couser *et al*. (1998) to obtain stable numerical computations. The other challenging part of this simulation was being able to reproduce wave breaking that occurred at the front of the bores. We described the results of the simulations conducted for one of the ship speeds corresponding to a depth-based Froude number F_h = 1.15. A 60 m long, 3.5 m wide and 0.114 m deep computational domain was set up with grid sizes $\Delta x = \Delta y$ = 0.05m for a total of 1201 points in the x direction and 71 points in the y direction. The lateral boundaries were fully reflecting while 0.5 m wide damping layers were placed at the upstream and downstream ends of the basin to absorb outgoing waves.

Numerical simulations were performed with time step size Δt = 0.015s, Smagorinsky coefficient C_s = 0.2 and bottom friction coefficient f_b = 0.01. A sample snapshot of the simulated water surface elevation is shown in Figure 18. The wave pattern initially starts off as a V-shaped wake. The reflected waves form Mach-stem waves along the channel walls that move towards the middle of the tank and eventually form a uniform long-crested solitary-type wave. Since the phase speed of solitary waves can be approximated by $\sqrt{g(h+H)}$, the solitary-type wave can travel faster than the ship over a narrow range of depth-based Froude numbers. This leads to the generation of a sequence of solitary-type waves ahead of the ship. The waves start to break for waves with crest elevations greater than approximately 60% of the water depth. This leads to the formation of an undular bore type profile ahead of the ship.

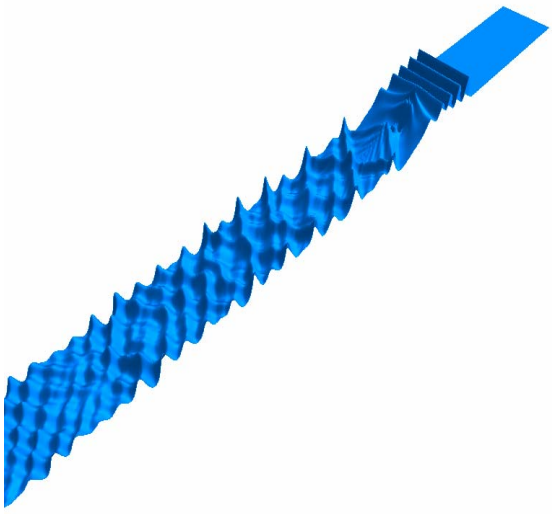

Figure 18: 3-D View of predicted wave pattern for a vessel travelling at Froude Number, F_h = 1.15 in narrow channel.

The measured and predicted water surface elevation time series at a gauge located at x= 44m, y = 0.72m are shown in Figure 19. The mean water level ahead of the ship increases while the water level along the sides of

the ship is reduced. The numerical model is able to predict the profile of the undular bore ahead of the ship. The predicted profile is sensitive to the wave breaking formulation and additional tests are being performed to yield the best formulation that works over a wide range of Froude numbers.

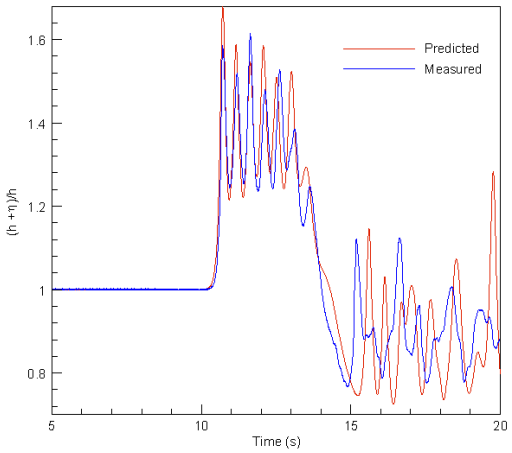

Figure 19: Comparison of time histories of measured and predicted free surface elevations at 0.72m from tank wall for a vessel travelling at Froude Number, $F_h = 1.15$.

CONCLUSIONS

A computationally-efficient numerical model has been developed to predict the waves generated by high-speed vessels traveling at subcritical, transcritical and supercritical speeds in shallow water. The model is based on a fully nonlinear set of Boussinesq-type equations for wave propagation over water of variable depth. The ship is represented in the far-field Boussinesq model by the vertical velocity field produced at the still water level by a distribution of sources over the body surface. Model-data comparisons have been conducted with two sets of laboratory experiments of ship-generated waves in both a wide and narrow channel. The numerical model was able to reasonably predict the ship-generated wave profiles excluding the extremely short-period diverging waves that are beyond the dispersive limit of the Boussinesq equations.

Acknowledgements

This work was supported the by the Coastal Inlets Research Program of the U.S. Army Corps of Engineers. The author would like to thank Profs. L. Doctors and T. Gourlay for providing the data from their laboratory experiments.

References

Beck, R.F., Cao, Y., and Lee, T.-H., "Fully nonlinear water wave computations using the desingularized method." Proc. 6th International Conference on Numerical Ship Hydrodynamics, Iowa City, Iowa, 1993, pp 3-20.

Couser, P., Wellicome J.F. and Molland, A.F., "An improved method for the theoretical prediction of the wave resistance of transom-stern hulls using a slender body approach", International Shipbuilding Progress, Vol. 45, No. 444, 1998, pp. 331-349.

Doctors, L.J., "The Influence of Viscosity on the wavemaking of a model catamaran", Proc. 18th International Workshop on Water Waves and Floating Bodies, Le Croisic, France, 2003, pp 12-1-12-4.

Ertekin, R.C., Webster, W.C. and Wehausen, J.V., "Waves caused by a moving disturbance in a shallow channel of finite width." Journal of Fluid Mechanics. Vol. 169, 1986, pp 275-292.

Gourlay, T.P., "The supercritical bore produced by a high-speed ship in a channel", Journal of Fluid Mechanics., Vol. 434, 2001, pp. 399-409.

Havelock, T.H. "The propagation of groups of waves in dispersive media, with application to waves on water produced by a travelling disturbance", Proc. Royal Society, London, Series A, Vol. 81, No. 549, 1908, pp. 398-430.

Nwogu, O., "Alternative form of Boussinesq Equations for nearshore wave propagation." Journal of Waterway, Port, Coastal and Ocean Engineering, ASCE, Vol. 119, No. 6, 1993, pp. 618-638.

Nwogu, O.G., "Numerical prediction of breaking waves and currents with a Boussinesq model.", Proc. 25th Int. Conf. on Coastal Eng., Orlando, ASCE, 1996, pp. 4807-4820.

Nwogu, O., and Demirbilek, Z., "BOUSS-2D: A Boussinesq wave model for coastal regions and harbors.", Tech. Rep. ERDC/CHL 01-25, U.S. Army Corps of Engineers Research and Development Center, Vicksburg, MS., 2001.

Robson, B.L., "Systematic series of high-speed displacement hull forms for naval combatants.", Trans. Royal Institute of Naval Architects, Vol. 130, 1988, pp. 241-252.

Tuck, E.O., "Shallow-water flows past slender bodies." Journal of Fluid Mechanics., Vol. **26**, 1966, pp. 81-95.

Wu, T.Y.-T. 1987. Generation of upstream advancing solitons by moving disturbances. Journal of Fluid Mechanics. Vol. 184, 1987, pp. 75-99.

Yeh, H.Y.H., “Series 64 Resistance Experiments on High-Speed Displacement Forms", Marine Technology, Vol. 2, No. 3, 1965, pp 248-272.